Magnetic resonance elastography with guided pressure waves

Marion Tardieu, Najat Salameh, Line Souris, David Rousseau, Laurène Jourdain, Hanadi Skeif, François Prévot, Ludovic de Rochefort, Denis Ducreux, Bruno Louis, et al.

Magnetic resonance elastography with guided pressure waves

Marion Tardieu[1], Najat Salameh[1], Line Souris[1], David Rousseau[2], Laurène Jourdain[1], Hanadi Skeif[1], François Prévot[1], Ludovic de Rochefort[1], Denis Ducreux[1], Bruno Louis[3], Philippe Garteiser[4], Ralph Sinkus[5], Luc Darrasse[1], Marie Poirier-Quinot[1], and Xavier Maître[1]

[1]Université Paris-Saclay, CEA, CNRS, Inserm, BioMaps, Orsay, France
[2]63Hz.fr - Conseil acoustique, Paris, France
[3]INSERM, U955, Equipe Biomécanique Cellulaire et Respiratoire, Créteil, France
[4]Laboratory of Imaging Biomarkers, UMR1149, INSERM-University Paris-Diderot, Paris, France
[5]Imaging Sciences & Biomedical Engineering Division, King's College, United Kingdom

Correspondence
BioMaps
Service Hospitalier Frédéric Joliot, CEA
4, place du général Leclerc
91401 Orsay cedex
France
Email: xavier.maitre@universite-paris-saclay.fr

Funding information
PHRC 13-033, AOR12016-P111109-g-brainMRE
MRE experiments were performed on the 1.5 T MRI platform of CEA/SHFJ, affiliated to the France Life Imaging network (grant ANR-11-INBS-0006)

Running Head
MRE with guided pressure waves

Running author
Tardieu et al.

Total words: 6941

KEYWORDS
Biomechanics, Pressure wave, Excitation, Magnetic Resonance Elastography, Magnetic Resonance Imaging, Brain

List of abbreviations
A: total amplitude
CV: Coefficient of Variation
G': storage shear modulus
G'': loss shear modulus
GRE: Gradient-Recalled Echo
MEG: Motion-Encoding Gradient
MRE: Magnetic Resonance Elastography
OSS: Octahedral Shear Strain
SE: Spin Echo
SNR: Signal-to-Noise Ratio
UNA: Uncertainty-normalized amplitude

Abstract

Magnetic resonance elastography aims at non-invasively and remotely characterizing the mechanical properties of living tissues. To quantitatively and regionally map *in vivo* the shear viscoelastic moduli, the technique must achieve proper mechanical excitation throughout the targeted tissues. Although it is straight forward, *ante manibus*, in close organs like the liver or the breast, which the practitioners clinically palpate already, it is somewhat fortunately highly-challenging to trick the natural protective barriers of remote organs like the brain. So far, mechanical waves have been induced in the latter two by shaking the surrounding cranial. Here, the skull was circumvented by guiding pressure waves inside the subject's buccal cavity so mechanical waves could propagate from within through the brainstem up to the brain. Repeatable, reproducible, and robust displacement fields were recorded in phantoms and *in vivo* by magnetic resonance elastography with guided pressure waves such that quantitative mechanical outcomes were extracted in the human brain.

1 Introduction

Magnetic resonance elastography (MRE) aims at non-invasively, remotely and quantitatively characterizing the mechanical properties of organs. The computed mechanical properties are sensitive biomarkers for pathophysiology and may reveal early changes in affected tissues. MRE consists in driving harmonic mechanical vibrations within the tissue – typically between 20 Hz and 200 Hz in human applications – and recording the inferred displacement fields by phase contrast MRI [1]. Tissue shear moduli are then computed using methods such as local frequency estimation [2], phase gradient approach [2], or wave equation inversion [2, 3, 4]. Today, MRE is implemented in clinical routine for staging fibrosis in patients with chronic liver diseases [5, 6]. It is being evaluated in cancer grading in the breast [3] or in the prostate [7] and it showed promising results in discriminating malignant from benign tumors. It has also been reported that early signs of tissue state changes can be detected with MRE and used to monitor thermal therapies [8, 9, 10].

One of the main limitations in the implementation of MRE comes from the ability to generate mechanical waves through the entire organ, especially when the latter is deeply located inside the body where wave propagation is hindered by natural barriers. The brain is especially protected by the skull as well as the meninges, which has required the development of original approaches to induce mechanical waves therein [11, 12, 13, 14, 15, 16, 17, 18, 19, 20]. In those studies, mechanical waves were induced by shaking the head along the two possible flexions: neck flexion was achieved either with a pillow-like vibrator applied under the subject's head [14, 21, 16, 20, 22, 23, 24] or with a cradle driven via a bar by a remote electromagnetic transducer [11, 25, 26, 27, 28, 19]; lateral flexion was promoted either with a bite bar driven by an electromagnetic actuator [29, 22, 12, 13, 30, 18] or by two passive actuator pads placed on each side of the skull near the pterions [15].

All these techniques attempt to generate mechanical waves that can propagate through the natural barriers of the cranium as well as the meninges. These waves must cope with reflections and losses at the interfaces, geometry and viscosity induced attenuation in the brain. Large mechanical amplitudes are thus required to produce rather low displacement field amplitudes as measured in both organs. These amplitudes were lower when the regions were deeper or when the vibration frequency was higher [12, 11, 22, 25, 30, 15, 16, 20, 31, 32]. Hence, most of the experiments were carried out using frequencies below 80 Hz to reduce viscosity-induced losses and to maintain wave amplitude throughout the organs [15, 33, 27, 18, 34, 24] even though higher mechanical frequencies might be required to match the scale and the complexity of the highly-structured brain [35].

In this work, we introduce new means of wave generation, which, instead of inducing mechanical waves through the protective barriers, makes use of the natural pathways inside the human body to guide remotely-generated pressure waves deep inside the organs. Shear wave amplitudes were maximized at the targeted site and a higher mechanical frequency range was explored. First, the pressure wave generator developed here was acoustically characterized to optimize pressure wave propagation along the resonant modes of our guiding system. Second, the pressure wave generator was implemented in phantoms and *in vivo* in the human brain. Displacement fields were recorded at excitation frequencies ranging from 43 Hz to 235 Hz in the brain. This approach was assessed in terms of repeatability, reproducibility, and robustness. MRE sensitivity was evaluated with respect not only to the amplitude of the displacement field generated inside the object of interest but also to its uncertainty, related to the signal-to-noise ratio (SNR) of the acquired images. We introduced the ratio between the total displacement field amplitude and the measurement uncertainty on the total displacement field amplitude as an indicator of the quality of the measured displacement field maps. This metric was used to set the validity conditions for MRE and it was compared to octahedral shear strain (OSS)-SNR introduced for this purpose by McGarry et al. [36]. Finally, the generation of mechanical waves inside the brain was challenged at high frequency in order to assess our technical limits to perform brain MRE with the guided pressure wave generator.

2 Methods

2.1 Guided pressure wave generator

2.1.1 Description

Mechanical excitation was induced in the targeted medium by pressure waves, which were remotely generated and guided to the subject or the phantom by the excitation chain depicted in Figure 1. Low-frequency sinusoidal waves, produced by a function generator (AFG 3021B, Tektronix, USA), were

amplified (power amplifier P2500S, Yamaha, Japan) and transduced into pressure waves by a 12" subwoofer (12NW100, B&C Speakers, Italy), hermetically-enclosed in a wooden cabinet. Pressure waves were transmitted onto the surface of targeted phantoms to be mechanically-characterized or into the subject's buccal cavity by an Altuglass® waveguide (22 mm inner diameter) connected to an antibacterial filter and an adaptation part or mouthpiece (Intersurgical, United Kingdom). In the buccal cavity, pressure waves hit the soft palate and traveled along the brainstem throughout the cerebral parenchyma during nasal respiration or along the airways down to the pulmonary parenchyma during oral breathing. The input sinusoidal waves were monitored before and after amplification with an oscilloscope (Tektronix, USA). The pressure level at the surface of the phantom or in the buccal cavity was recorded by an optical pressure sensor (OPP-M, OpSens, Canada) connected via luer lock to the antibacterial filter. It was continuously monitored over the experiments (SoftProSens software, OpSens, Canada). The subwoofer temperature was controlled by a temperature sensor (Model 70, Cryomagnetics inc., USA) while the wooden enclosure was water-cooled to prevent coil overheating and to maintain the transducer efficiency over the long experimental runs. The amplification and transduction unit was located in a technical room, behind the examination room, along the axis of the imaging magnet, beyond the 5 Gauss line. The driving and monitoring units were located in the console room so the frequency and the amplitude of the input sinusoidal wave could be selected and the applied pressure wave could be supervised along the running MR acquisitions.

2.1.2 Excitation chain characterization

The excitation chain is characterized by the resonance modes of the overall system, which comprises the subwoofer, the waveguide and the buccal cavity. Hence, the applied pressure is enhanced when the frequency of the input sinusoidal wave matches one of the acoustic resonance frequencies of the system. As the dimensions of the waveguide are way greater than the other involved parts, the system resonances are mainly governed by the waveguide modes. The acoustic resonance frequencies of the system, f_n, correspond to closed tube resonances, such as:

$$f_n = \frac{(2n-1)\,C_0}{4L}, \tag{1}$$

where n is the resonance mode number ($n \in \mathbb{N}$), C_0 is the speed of sound in air ($340.5\,\mathrm{m \cdot s^{-1}}$ at 15 °C) and L is the length of the waveguide.

The effective frequency response of the excitation chain at the end of the waveguide was recorded with the calibrated pressure sensor in a closed configuration using a data acquisition board (BNC-2120, National Instruments, USA) driven by Matlab (The MathWorks Inc., Natick, MA, USA). The frequency of the input sinusoidal wave was swept from 10 Hz to 400 Hz. The measurements were carried for different waveguide lengths: no tube, 1.10 m, 1.70 m, 2.10 m and 2.50 m and for ten input voltages (before amplification): from $1\,\mathrm{V_{RMS}}$ to $10\,\mathrm{V_{RMS}}$.

For multi-frequency MRE experiments, the frequency response of the system was measured when three harmonic frequencies were simultaneously applied: 32 Hz, 64 Hz and 96 Hz, for a 2.50 m waveguide at $8\,\mathrm{V_{RMS}}$. For this length of waveguide, only 32 Hz and 96 Hz frequencies were close to a resonance mode of the system (Figure 2 a).

2.2 MRE data quality

2.2.1 General considerations

The quality of the recorded displacement field maps strongly depends on the mechanical wave amplitude, A, the sensitivity to motion of the MR acquisition, namely the amplitude and duration of the motion-encoding gradients, and the uncertainty on the recorded MR phase, i.e. the signal-to-noise ratio (SNR) of the measurement.

First, octahedral shear strain (OSS)-SNR, based on the measure of the principal shear component of the strain, was used to estimate the quality of the recorded displacement field maps as formerly performed [17, 19, 23]. Second, the quality of MRE data was assessed through the ratio between the total amplitude and the measurement uncertainty of the total amplitude, the uncertainty-normalized amplitude UNA = $\langle A/\Delta A \rangle$. Both approaches with OSS-SNR and UNA were then compared.

2.2.2 From measured phase to displacement fields

The overall phase Φ of the acquired MR signal recorded during the application of the motion-encoding gradients — as well as the motion sensitivity — is determined by the applied MR sequence. Here, two 3D-motion-sensitized sequences were implemented to check the mechanical excitation with clinically-available standard acquisition protocols. The first one, based on a spin-echo (SE) sequence, made use of two sinusoidal bipolar motion-encoding gradients (MEGs), $\vec{G}$, which duration T_{MEG} was equal to the mechanical excitation period T_{exc} [37]. The second one, based on a gradient-recalled echo (GRE) sequence, made used of only one trapezoidal bipolar MEG, which duration T_{MEG} was shorter than the mechanical excitation period [38, 39]. The displacement field $\vec{u}$ at location $\vec{r}$ and mechanical phase θ is encoded onto the phase Φ of the acquired MR signal according to the following equations:

$$\Phi\left(\vec{r},\theta\right) = \frac{\gamma N_{\mathrm{MEG}} T_{\mathrm{exc}} \vec{G} \cdot \vec{u}\left(\vec{r},\theta\right)}{2}, \text{ for SE MRE,} \tag{2}$$

and

$$\Phi(\vec{r},\theta) = \gamma T_{\mathrm{MEG}} \vec{G} \cdot \vec{u}\left(\vec{r},\theta\right) \frac{\sin\left(\pi \frac{T_{\mathrm{MEG}}}{T_{\mathrm{exc}}}\right)}{\pi \cdot \left(1 - \left(\frac{T_{\mathrm{MEG}}}{T_{\mathrm{exc}}}\right)^2\right)}, \text{ for GRE MRE,} \tag{3}$$

where γ is the gyromagnetic ratio and N_{MEG}, the number of bipolar MEG.

2.2.3 Uncertainty-normalized amplitude

The measurement uncertainty of the MR phase $\Delta\Phi_i$ along the motion-encoding direction i ($i \in \{x, y, z\}$) is a function of the signal-to-noise ratio along the same direction (SNR_i) according to [40, 41] :

$$\Delta\Phi_i = \arctan\left(\frac{1}{\mathrm{SNR}_i}\right). \tag{4}$$

Following Equations 2 and 3, the measurement uncertainty of the displacement field amplitude ΔA_i along i, ($i \in \{x, y, z\}$), is:

$$(\Delta A_i)_{\mathrm{SE}} = \arctan\left(\frac{1}{\mathrm{SNR}_i}\right) \frac{2}{\gamma N_{\mathrm{MEG}} T_{\mathrm{exc}} G_i}, \text{ for SE MRE,} \tag{5}$$

and

$$(\Delta A_i)_{\mathrm{GRE}} = \arctan\left(\frac{1}{\mathrm{SNR}_i}\right) \frac{\pi \cdot \left(1 - \left(\frac{T_{\mathrm{MEG}}}{T_{\mathrm{exc}}}\right)^2\right)}{\gamma T_{\mathrm{MEG}} G_i \sin\left(\pi \frac{T_{\mathrm{MEG}}}{T_{\mathrm{exc}}}\right)}, \text{ for GRE MRE.} \tag{6}$$

The uncertainty of the total amplitude of the displacement field, $A = \left(A_x^2 + A_y^2 + A_z^2\right)^{1/2}$, is then given by:

$$\Delta A = \frac{A_x \Delta A_x + A_y \Delta A_y + A_z \Delta A_z}{A}. \tag{7}$$

Finally, the uncertainty-normalized amplitude is:

$$\mathrm{UNA} = \frac{A_x^2 + A_y^2 + A_z^2}{A_x \Delta A_x + A_y \Delta A_y + A_z \Delta A_z}. \tag{8}$$

2.3 MRE experiments

2.3.1 Data acquisition and image reconstruction

For each experimental setup, the specific excitation chain was fully calibrated before any MRE acquisitions. The calibration procedure consisted in characterizing the frequency response of the system close to the phantom surface or the subject's mouth, at the antibacterial filter up to 400 Hz. Thereby, either optimal vibration frequencies could be selected, or the waveguide length could be adapted to match one of the system resonance frequencies to the desired vibration frequency (Eq. 1).

MRE with guided pressure waves was performed, first, on a phantom (p) to alleviate time- and motion-related limitations, and, second, *in vivo* on human brain (b). Repeatability, robustness, and reproducibility of MRE with guided pressure waves were evaluated for both phantom and human brain in a 1.5 T MRI system (Achieva, Philips Healthcare, Netherlands) with the two different SE and GRE MRE sequences. For both sequences, the MEG amplitude was $21\,\mathrm{mT}\cdot\mathrm{m}^{-1}$; MEGs were synchronized with the pressure wave and data were acquired at four time offsets within the mechanical period, for each of the three spatial directions. After initial phase unwrapping, storage (G') and loss (G'') shear moduli were extracted by inversion of the Helmholtz equation, which governs the rotational field of the acquired three-dimensional displacement field maps [3]. Every measurement averages and standard deviations were spatially calculated over the entire imaged phantom or organ, unless otherwise specified.

Repeatability Repeatability experiments were set up to evaluate the variability of MRE outcomes using guided pressure waves by repeating five times the same MRE acquisition protocol, for both MRE sequences. Coefficient of variation was used to determine this repeatibility and is defined as standard deviation divided by the mean. Three-dimensional mean and coefficient of variation maps of the shear moduli, $\langle G'\rangle$, $\langle G''\rangle$, $\mathrm{CV}(G')$ and $\mathrm{CV}(G'')$, were computed, on a voxel-by-voxel basis, over the five repeated acquisitions.

Robustness Robustness experiments challenged the stability and the linearity of MRE using guided pressure waves by acquiring MRE data over a range of excitation input voltages. These experiments also allowed to establish the ability of the excitation system to generate pressure waves with sufficiently-high pressure at the surface of the phantom or in the buccal cavity so propagating shear waves could be generated throughout the medium and the biological tissues with a large enough amplitude. For each input voltage, mean storage and loss moduli, $\langle G'\rangle_{p\text{ or }b}$ and $\langle G''\rangle_{p\text{ or }b}$, over the entire acquired MRE phantom (p) or brain (b), were plotted as a function of the mean OSS-SNR and the mean UNA in order to define threshold values from which the mechanical parameters can be accurately reconstructed. These plots were fitted by an exponential growth and the threshold values were calculated from the plateau value of the fitted curves, leaving a mean error margin equal to the measurement uncertainties of G' and G'' deduced from the repeatability experiments.

Reproducibility Reproducibility experiments aimed at knowing the dependence of the MRE outcomes with the setting of the excitation system. MRE data were acquired after several installations of the experimental setup on the same phantom and on the same subject either on the same day or on different days. Intra-subject coefficients of variation were extracted to assess reproducibility.

2.3.2 Phantom MRE

MRE was performed in a multi-modality phantom (Model 073, Computer Imaging Reference Systems, USA) with a background made in Zerdine®-based emulsion with mimicking cystic and dense masses. Its compressional behavior was assimilated to fatty breast tissue. Even though the manufacturer did not specify any shear modulus, the background of such a phantom could be assumed to be largely elastic [42]. However, due to the presence of the additional masses, the shear loss modulus could not be neglected due to potential scattering effects at the interface between mechanically-different regions. For every MRE experiment, the MR-signal was recorded from the whole phantom with two flexible coils (SENSE Flex-M, Philips Healthcare, The Netherlands). Acquisition matrix size was $(64\times64\times38)$ with an isotropic voxel size of $(2\,\mathrm{mm})^3$ and a pressure wave frequency of 85 Hz. Other sequence parameters are presented in Table 1.

Table 1: Sequence parameters in phantom MRE acquisitions

Parameter	SE MRE	GRE MRE
Repetition and echo times TR/TE	2235/41 ms	450/9.2 ms
MEG duration $T_{\mathbf{MEG}}$	$T_{\mathrm{exc}}=1/f$	8.2 ms
Total acquisition time T_{Acq}	24 min	6 min

To challenge repeatability, a pressure level of $(162\,\mathrm{dB\,SPL})_{\mathrm{SE}}$ and $(165\,\mathrm{dB\,SPL})_{\mathrm{GRE}}$ was applied at the surface of the phantom. For the robustness study, the pressure level ranged between 133 dB SPL and 164 dB SPL. To challenge reproducibility, the acquisitions for the robustness experiments were performed

twice over five months for the two SE and GRE MRE sequences. Over the long experimental runs and the long storage times, the shear viscoelasticity of the phantom varied; so, for the sake of comparison, data plots and fitting curves were normalized by the plateau value of each fitted exponential curves.

2.3.3 *In vivo* brain MRE

Brain MRE were performed on a healthy volunteer (man, 44 years old) as part of a clinical research protocol (PHRC 13-033, AOR12016-P111109-g-brainMRE) approved by the local ethical committee. The acquisitions were performed using a standard 8-channel head coil (Sense Head coil, Philips Healthcare, The Netherlands) at mechanical frequencies close to one of the acoustic resonant frequencies of the guided-pressure wave system with the sequence parameters presented in Table 2.

Table 2: Sequence parameters in brain MRE acquisitions for repeatability, robustness, and reproducibility experiments

Parameters	Repeatability		Robustness	Reproducibility
Sequence	SE MRE	GRE MRE	SE MRE	GRE MRE
Acquisition matrix size	$(80 \times 80 \times 7)$	$(128 \times 128 \times 12)$	$(80 \times 80 \times 12)$	$(96 \times 96 \times 52)$
Isotropic voxel size	$(2.94\,\mathrm{mm})^3$	$(2\,\mathrm{mm})^3$	$(2.94\,\mathrm{mm})^3$	$(2.75\,\mathrm{mm})^3$
Pressure wave frequency f	83 Hz	83 Hz	79 Hz	83 Hz
Repetition and echo times TR/TE	422/42 ms	147/9.2 ms	760/44 ms	629/9.2 ms
MEG duration $T_{\mathbf{MEG}}$	$T_{\mathrm{exc}} = 1/f$	8.2 ms	$T_{\mathrm{exc}} = 1/f$	8.2 ms
Acquisition time T_{Acq}	4 min 48 s	3 min	8 min 37 s	10 min 49 s

For repeatability and robustness experiments, the slices were located between the cerebellum and the ventricles where the displacement fields are expected to be strong. For robustness experiments, the acquisition was repeated thirteen times for different input voltages, from 0 to $38.4\,\mathrm{V_{RMS}}$, to achieve a pressure level up to 164.4 dB SPL. For reproducibility experiments, the MR-signal was recorded from the whole brain three times: twice the same day with a break out of the scanner and identical positioning of the subject's head (acq.1 and acq.2) and once a month later with the subject's head rotated to the left (acq.3). Pressure levels were recorded at the subject's mouth at $(165.0\,\mathrm{dB\,SPL})_{acq.1}$, $(163.7\,\mathrm{dB\,SPL})_{acq.2}$ and $(163.0\,\mathrm{dB\,SPL})_{acq.3}$. To compare these three acquisitions, data from acq.1 and acq.3 were first spatially-normalized to acq.2 with SPM8 [1]. Then, they were phase-normalized to express the corresponding displacement field maps in the reference frame given by the motion encoding direction of acq. 2. [43, 44]. Storage and loss modulus maps were also compared between the three acquisitions and mean values $\langle G' \rangle_b$ and $\langle G'' \rangle_b$ as well as coefficients of variation $\mathrm{CV}(G')_b$ and $\mathrm{CV}(G'')_b$ were calculated over the brain.

An additional set of brain MRE acquisitions were performed with the SE MRE sequence to characterize the pressure-wave-induced displacement fields at higher frequencies, selected close to the acoustic resonant frequencies of the system: 174 Hz, 200 Hz and 235 Hz. The acquisition matrix was $(80 \times 80 \times 7)$ with an isotropic voxel size of $(2.94\,\mathrm{mm})^3$. To maintain the measurement sensitivity with the increasing excitation frequency, the number of MEG, N_{MEG}, was increased from 2 to 8 (174 Hz), 14 (200 Hz), and 18 (235 Hz). Associated TR/TE were $(563/60\,\mathrm{ms})_{174\,\mathrm{Hz}}$, $(1016/83\,\mathrm{ms})_{200\,\mathrm{Hz}}$ and $(1130/89\,\mathrm{ms})_{235\,\mathrm{Hz}}$. Total acquisition times were $(6\,\mathrm{min}\ 24\,\mathrm{s})_{174\,\mathrm{Hz}}$, $(11\,\mathrm{min}\ 24\,\mathrm{s})_{200\,\mathrm{Hz}}$, and $(12\,\mathrm{min}\ 50\,\mathrm{s})_{235\,\mathrm{Hz}}$. Pressure levels of the incoming guided pressure waves were recorded at $(167.2\,\mathrm{dB\,SPL})_{174\,\mathrm{Hz}}$, $(165.6\,\mathrm{dB\,SPL})_{200\,\mathrm{Hz}}$ and $(164.4\,\mathrm{dB\,SPL})_{235\,\mathrm{Hz}}$.

Additional data sets were acquired in the same conditions on the same subject at 52 Hz, 113 Hz, and 144 Hz as well as on two other volunteers (men 27 and 44 y/o) at 63 Hz and 72 Hz respectively. To further reveal the penetration of high frequency shear waves in the cerebral and cerebellar tissues, MRE sensitivity was improved with increased MEG amplitude, $33\,\mathrm{mT} \cdot \mathrm{m}^{-1}$, at 174 Hz, and 235 Hz. They are available as supplementary materials.

[1] Statistical Parametric Mapping, UCL, `http://www.fil.ion.ucl.ac.uk/spm/`

3 Results

3.1 Transducer characterization

Figure 2.a shows the frequency response curves of the pressure wave generator system for five different waveguide lengths with an input voltage of $8\,V_{RMS}$. The output pressure level is enhanced up to 30 dB SPL at the frequencies of the waveguide resonant modes. The frequency of the first system resonance mode is lowered when the length of the waveguide is increased and the resonant frequencies verify Eq. 1. By tuning the waveguide length, it is then possible to maximize the output pressure level at the surface of the targeted system or in the subject's buccal cavity for any selected excitation frequency.

For six resonance frequencies, Figure 2.b shows the pressure level versus the input voltage applied to the excitation chain in logarithmic scales.

Figure 2 also shows the harmonic response for three harmonic frequencies (32 Hz, 64 Hz, and 96 Hz) applied together (2.c) and separately (2.d), for a waveguide of 250 cm. The responses are similar and reveal pressure levels, with three harmonics, of $(163\,\text{dB SPL})_{32\text{Hz}}$, $(151.5\,\text{dB SPL})_{64\,\text{Hz}}$ and $(167.8\,\text{dB SPL})_{96\,\text{Hz}}$. These plots also exhibit the presence of harmonic distortions, such as the one at 48 Hz with a pressure level of 138.5 dB SPL. These harmonic distortions are related to the 96 Hz excitation, frequency close to the natural frequency of the system.

3.2 Phantom MRE acquisitions

Repeatability The SNR mean values and coefficients of variation, measured voxel-by-voxel, over the five repeated acquisitions, are:

$$\langle \text{SNR} \rangle_{p,\text{SE}} = (63.9 \pm 9.5)\,,\ \text{CV}(\text{SNR})_{p,\text{SE}} = (0.01 \pm 0.01)$$
$$\langle \text{SNR} \rangle_{p,\text{GRE}} = (14.5 \pm 2.7)\,,\ \text{CV}(\text{SNR})_{p,\text{GRE}} = (0.02 \pm 0.02)$$

They yield repetition uncertainties of the total amplitude of:

$$\langle \Delta A \rangle_{p,\text{SE}} = (0.5 \pm 0.3)\,\mu\text{m},\ \text{CV}(\Delta A)_{p,\text{SE}} = (0.30 \pm 0.17)$$
$$\langle \Delta A \rangle_{p,\text{GRE}} = (4.4 \pm 1.9)\,\mu\text{m},\ \text{CV}(\Delta A)_{p,\text{GRE}} = (0.42 \pm 0.17).$$

For each displacement field data set, G' and G'' maps were reconstructed to infer mean and coefficient of variation maps over the five repeated acquisitions. G' as well as A maps are represented in figure 3.a for SE and GRE sequences. Averaged value of mean and coefficient of variation maps of G', G'' and A are given in Table 3, for both MRE sequence..

Table 3: Voxel-by-voxel mean shear storage and loss moduli, $\langle G' \rangle_p$ and $\langle G'' \rangle_p$, and mean total amplitude $\langle A \rangle_p$, with related coefficients of variation over five repeated acquisitions averaged over the phantom with SE and GRE MRE sequences.

	G'		G''		A	
	$\langle G' \rangle_p$ (kPa)	CV_p	$\langle G'' \rangle_p$ (kPa)	CV_p	$\langle A \rangle_p$ (µm)	CV_p
SE MRE	3.1 ± 1.2	0.07 ± 0.06	2.3 ± 1.0	0.08 ± 0.06	47.4 ± 43.3	0.03 ± 0.01
GRE MRE	2.8 ± 1.0	0.13 ± 0.11	2.1 ± 0.9	0.14 ± 0.10	77.9 ± 79.7	0.07 ± 0.02

Displacement field maps for one of the five repeated acquisitions are presented in figure 3.b for the SE and GRE MRE sequences, along the x, y, and z directions. The corresponding T_1-weighted image and storage modulus maps are also depicted in this figure. For both the displacement field maps and the storage modulus maps, similar wave patterns are captured by the two MRE sequences. For these two acquisitions, storage modulus mean values over the phantom are: $\langle G' \rangle_{p,\text{SE}} = (3.0 \pm 1.2)$ kPa and $\langle G' \rangle_{p,\text{GRE}} = (2.6 \pm 1.4)$ kPa.

Robustness Figure 4 (top row) shows the extracted normalized mean storage modulus, $\langle G' \rangle$, of the phantom as a function of $\langle \text{UNA} \rangle$ (a) and $\langle \text{OSS-SNR} \rangle$ (b). Both plots follow an exponential growth and plateaus are reached with thresholds of $\langle \text{UNA} \rangle_{p,\text{SE}} = 16.2$, $\langle \text{UNA} \rangle_{p,\text{GRE}} = 13.0$, $\langle \text{OSS-SNR} \rangle_{p,\text{SE}} = 6.6$, and $\langle \text{OSS-SNR} \rangle_{p,\text{GRE}} = 4.2$, which corresponds to a mean total amplitude $\langle A \rangle_{p,\text{GRE}} > 22.5\,\mu\text{m}$ (149.4 dB SPL) for the GRE MRE sequence and $\langle A \rangle_{p,\text{SE}} > 6.0\,\mu\text{m}$ (144.8 dB SPL) for the SE MRE sequence. Higher $\langle \text{OSS-SNR} \rangle_p$ values are found for the GRE MRE acquisition.

Reproducibility Acquisition reproducibility was assessed using the robustness tests where the experiments were repeated at different time points. The overall results of mean storage modulus are displayed in Figure 4.a and b. Intra-subject coefficients of variation were measured between normalized robustness acquisition data for which $\langle \text{UNA} \rangle > 16.2$ for SE MRE sequence and $\langle \text{UNA} \rangle > 13.0$ for GRE MRE sequence: $\text{CV}(G')_{\text{SE}} = 4\%$ and $\text{CV}(G')_{\text{GRE}} = 3\%$

3.3 Brain MRE acquisitions

Repeatability On a voxel-by-voxel basis, the SNR values averaged over the five repeated acquisitions in the same subject, $\langle \text{SNR} \rangle$, and the corresponding coefficients of variation, CV(SNR), averaged over the brain, are:

$$\langle \text{SNR} \rangle_{b,\text{SE}} = (17.1 \pm 5.4)\,,\ \text{CV}(\text{SNR})_{b,\text{SE}} = (0.07 \pm 0.05)$$
$$\langle \text{SNR} \rangle_{b,\text{GRE}} = (5.4 \pm 1.4)\,,\ \text{CV}(\text{SNR})_{b,\text{GRE}} = (0.07 \pm 0.04)$$

for SE and GRE MRE sequences respectively, and leading to the following total amplitude uncertainties:

$$\langle \Delta A \rangle_{b,\text{SE}} = (1.4 \pm 1.0)\,\mu\text{m},\ \text{CV}(\Delta A)_{b,\text{SE}} = (0.10 \pm 0.05)$$
$$\langle \Delta A \rangle_{b,\text{GRE}} = (9.8 \pm 4.7)\,\mu\text{m},\ \text{CV}(\Delta A)_{b,\text{GRE}} = (0.06 \pm 0.03).$$

Mean and coefficient of variation maps of the shear moduli and total amplitude were computed from G', G'' and A maps of the five repeated acquisitions, for both SE and GRE sequences (Figure 5). The inferred measurement mean values and coefficient of variation of the shear moduli averaged over the brain are presented in Table 4. On a voxel-by-voxel basis, the repeatability of G' falls within 17% (SE and GRE) and of G'' within 20% (SE) and 24% (GRE) whereas overall mean values differ by a factor of four between SE and GRE shear and storage moduli.

Table 4: Voxel-by-voxel mean shear storage and loss moduli, $\langle G'_v \rangle_b$ and $\langle G''_v \rangle_b$, and total amplitude $\langle A \rangle_b$, with related coefficients of variation CV over five repeated acquisitions on the same volunteer averaged over the brain with SE and GRE MRE sequences.

	G'		G''		A	
	$\langle G' \rangle_b$ (kPa)	CV_b	$\langle G'' \rangle_b$ (kPa)	CV_b	$\langle A \rangle_b$ (µm)	CV_b
SE MRE	3.1 ± 1.0	0.17 ± 0.10	2.2 ± 0.7	0.17 ± 0.09	8.3 ± 4.4	0.10 ± 0.04
GRE MRE	0.8 ± 0.2	0.20 ± 0.08	0.5 ± 0.2	0.24 ± 0.09	16.0 ± 9.2	0.26 ± 0.08

Robustness Raw displacement field maps, $\vec{u}$, along the x (right-left), y (anteroposterior), and z (feet-head) directions are provided along the mechanical cycle in Figure S1 of the supplementary materials. Magnitude image presented a mean SNR over the acquired brain volume of $\langle SNR \rangle_{b,162.9\,\text{dB SPL}} = (30.9 \pm 7.7)$ leading to a measurement uncertainty of the total amplitude of $\langle \Delta A_{\text{tot}} \rangle_{b,162.9\,\text{dB SPL}} = (0.6 \pm 0.2)$ µm, for a mean total amplitude of $\langle A \rangle_{b,162.9\,\text{dB SPL}} = (7.4 \pm 4.8)$ µm.

Figures 4.c and d present G' and G'' as a function of $\langle \text{UNA} \rangle$ and $\langle \text{OSS-SNR} \rangle$ with their respective fitted curves. As for the MRE phantom study, the measured data follow an exponential growth with $\langle \text{UNA} \rangle$ and $\langle \text{OSS-SNR} \rangle$, and the shear moduli reach plateau values $\langle G' \rangle_b = 2.7\,\text{kPa}$ and $\langle G'' \rangle_b = 1.8\,\text{kPa}$, with thresholds computed from measurement uncertainties of shear moduli at $\langle \text{UNA} \rangle_{b,G'} = 3.9$ and $\langle \text{UNA} \rangle_{b,G''} = 3.1$; $\langle \text{OSS-SNR} \rangle_{b,G'} = 3.3$ and $\langle \text{OSS-SNR} \rangle_{b,G''} = 3.1$.

Reproducibility Acquisitions present similar mean SNR values ($28 < \langle SNR \rangle < 34$), which lead to similar measurement uncertainty of displacement field (1.4 µm $< \langle \Delta A \rangle <$ 1.7 µm), for similar mean displacement field amplitude (13 µm $< \langle A \rangle <$ 22 µm) as summarized in Table 5.

Table 5: Mean SNR, mean displacement field amplitude, and associated mean displacement field uncertainty over the whole brain for three different experimental runs performed on the same subject.

Acquisitions	1	2	3
$\langle SNR \rangle$	(28.5 ± 6.5)	(33.8 ± 6.9)	(30.9 ± 7.7)
$\langle A \rangle$	(13.2 ± 6.8) µm	(21.4 ± 6.3) µm	(22.0 ± 12.7) µm
$\langle \Delta A \rangle$	(1.6 ± 1.0) µm	(1.4 ± 0.5) µm	(1.5 ± 1.0) µm

Figure 6 shows amplitude maps for the x (right-left), y (antero-posterior), and z (feet-head) encoded directions, for a sagittal slice. Total amplitude maps are also shown for the three acquisitions with total amplitude up to 40 µm. Mean and coefficient of variation maps over the three acquisitions are presented for each encoded direction. All these maps show similar amplitude patterns for the three acquisitions, with maximum amplitudes, for directions x and y, at the tentorium cerebelli, and, for the direction z at the superior cerebellar peduncle and in the frontal lobe.

Storage and loss moduli present similar patterns across acquisitions, with maximum values in the white matter, midbrain and tentorium cerebelli for G', and midbrain and superior part of the cerebellum anterior lobe for G'' (Figure 7). For each acquisition, G' and G'' values calculated over the entire brain range between 1.3 kPa and 2.1 kPa while UNA varies from 8 to 16 as reported in Table 6. Intra-subject coefficients of variation were measured as 16% for G' and 19% for G''. Pixels with values below the UNA threshold, as defined above, are excluded and marked with black and white stripes.

Table 6: Mean values of G' and G'' over the whole brain for three different experimental runs performed on the same subject with associated UNA.

Acquisitions	1	2	3
$\langle G' \rangle$	(2.0 ± 0.7) kPa	(2.1 ± 0.6) kPa	(2.0 ± 0.7) kPa
$\langle G'' \rangle$	(1.2 ± 0.5) kPa	(1.3 ± 0.5) kPa	(1.3 ± 0.5) kPa
$\langle \mathrm{UNA} \rangle$	(8.5 ± 3.5)	(15.6 ± 4.0)	(16.0 ± 6.4)

Frequency study Raw displacement field maps, $\vec{u}$, along the x (right-left), y (anteroposterior), and z (feet-head) directions are provided for every frequency and acquired slice along the mechanical cycle in Figure S1 of the supplementary materials. Figure 8 shows A, G' and G'' maps for a transverse slice located above the cerebellum. Extracted mean total amplitude are $\langle A \rangle_{b,174\,\mathrm{Hz}} = (5.5 \pm 3.6)$ µm, $\langle A \rangle_{b,200\,\mathrm{Hz}} = (3.8 \pm 2.6)$ µm and $\langle A \rangle_{b,235\,\mathrm{Hz}} = (2.6 \pm 1.8)$ µm, mean storage modulus: $\langle G' \rangle_{b,174\,\mathrm{Hz}} = (7.6 \pm 4.4)$ kPa, $\langle G' \rangle_{b,200\,\mathrm{Hz}} = (9.2 \pm 5.4)$ kPa and $\langle G' \rangle_{b,235\,\mathrm{Hz}} = (11.9 \pm 6.6)$ kPa, and mean loss modulus: $\langle G'' \rangle_{b,174\,\mathrm{Hz}} = (5.6 \pm 3.3)$ kPa, $\langle G'' \rangle_{b,200\,\mathrm{Hz}} = (6.8 \pm 3.5)$ kPa and $\langle G'' \rangle_{b,235\,\mathrm{Hz}} = (9.1 \pm 4.5)$ kPa. The phase accumulation with a number of bipolar motion-encoding gradients greater than two yielded to UNAs greater than the threshold determined during the robustness experiments: $\langle \mathrm{UNA} \rangle_{b,174\,\mathrm{Hz}} = 10.6 \pm 6.8$, $\langle \mathrm{UNA} \rangle_{b,200\,\mathrm{Hz}} = 13.4 \pm 9.4$ and $\langle \mathrm{UNA} \rangle_{b,235\,\mathrm{Hz}} = 9.9 \pm 7.0$. Pixel values below the UNA threshold are indicated in Figure 8. For all the acquired slices, they represent 4% (174 Hz), 1% (200 Hz) and 13% (235 Hz) of the total pixel number. Corresponding OSS-SNR values were: $\langle \text{OSS-SNR} \rangle_{b,174\,\mathrm{Hz}} = 7.33 \pm 7.71$, $\langle \text{OSS-SNR} \rangle_{b,200\,\mathrm{Hz}} = 8.26 \pm 8.12$ and $\langle \text{OSS-SNR} \rangle_{b,235\,\mathrm{Hz}} = 8.24 \pm 8.32$.

4 Discussion

In this work, we introduced an original guided pressure wave generator for MRE. The system was fully characterized so its frequency range, frequency modes, and pressure level were determined. In the context of MRE, the pressure waves were guided to the surface of the phantom or, here, in the subject's mouth to mechanically probe brain tissue. Three tests were successfully performed both in phantoms and *in vivo*: a repeatability test to challenge the system consistency by successively repeating several times the same experimental protocol; a reproducibility test to challenge system repositioning; and a robustness test to challenge the linearity of the system with the driving voltage and determine wave amplitude-related conditions of validity for MRE.

The system proved to be linear over the required frequency and amplitude ranges. Even though the frequency response curves presented some residual harmonic distortions, such system is suitable for multifrequency MRE studies as a time-domain Fourier transform is applied to reconstruct shear wave maps [39]. The use of a waveguide is marked by resonance modes. These modes, characterized for each configuration along the experimental protocol, can be utilized to enhance the output pressure levels and gains up to 30 dB are obtained at the system resonant frequencies. It is then possible with the current design to achieve mechanical excitations at frequencies up to 400 Hz. The frequencies of these modes essentially depend on the waveguide length and can easily be tuned by changing this length. Hence, to optimally implement mechanical excitation with guided pressure waves, it is advised to run a characterization process with frequency sweep, as described above, when the setup is changed, say when the length of the waveguide, the adapting part, or the probed system is changed. It is then safe

to monitor the pressure close to the surface of the excited tissue or at the subject's mouth in order to assess its proper functioning over the MRE acquisition.

The robustness of the excitation system was ascertained by both characterization measurements and MRE experiments. Above specific UNA threshold values, shear storage and loss moduli could be repeated and reproduced in the phantom and in the brain so to produce quantitative mechanical properties. Indeed, one of the main advantages of guided pressure wave excitation relies in the inherent reproducibility of the generated displacement field patterns *in vivo* as waves are guided in the subject along the anatomical structures and the wave amplitude only depends on the effective setup by the coupling between the waveguide and the buccal cavity. The patterns of the displacement fields are similar whatever the position of the subject's head is in the MRI system. As the values of the extracted viscoelastic moduli are usually influenced by the displacement field patterns when standard isotropic reconstruction is applied [23], the reproducibility of the displacement fields, regardless of the excitation positioning, is required to provide absolute quantitation for longitudinal studies or subject-to-subject comparison. Thereof, brain mechanical atlases for healthy and disease subjects can be more favorably envisioned.

The brain is composed of two well-separated hemispheres with multiple highly-folded viscous structures and large membrane interfaces. Therein, shear waves are reflected and attenuated [15, 45]. The wave amplitude decreases from the periphery to the center of the organ [22, 11, 25, 30, 17]. Moreover, when waves are generated through the skull and the meninges into the brain, compressional waves spread around the cranial bone and additional scattering and attenuation damp the transmitted shear waves. Finally, attenuation increases with the mechanical frequency, which usually impedes the generation of waves with high mechanical frequencies, hence low shear wavelengths. The usual working frequency range is then $30 - 60\,\mathrm{Hz}$ such that the expected associated wavelengths in the brain are greater than a few centimeters. They are larger than most of the brain structures and small anatomical regions – like the pituitary gland – cannot be reasonably probed with commonly-implemented spatial resolutions, which lead to undersampled shear wavelength [35]. Guiding shear waves through natural pathways from within alleviate not only primary attenuation through the protective brain barriers but also the brain tissue attenuation as the main source is already inside the brain along the stem. Here, the displacement field maps sustain generation of shear waves over the entire brain with sufficient amplitudes to correctly compute shear storage and loss modulus maps even deep inside – between the cerebellum and the ventricles – at frequencies up to $174\,\mathrm{Hz}$ whereas brain MRE was limited so far to $100\,\mathrm{Hz}$ [14, 30, 18, 16]. Following the frequency spectrum and mode shapes of a human head–neck model, induced higher frequency pressure waves achieved here at 200 Hz and 235 Hz are expected to feed higher compressional modes that do not encompass the whole brain anymore but start being localized with favored lateral flexion of the nasal lateral cartilage and lateral motion of mandible [46]. With building brain mechanical atlases in mind, whole-brain studies with high spatial resolution should be performed at high excitation frequency. They call for long acquisition times and therefore a comfortable mechanical excitation [17]. With guided pressure wave, vibrational discomfort can be diminished provided the mouth piece is mechanically decoupled from the waveguide and the tube associated propagating modes are damped. Yet, when the function generator output is switched on at the start of the MRE sequence, the rapid pressure buildup in the buccal cavity is usually surprising. Gradual pressure level can then be implemented and subjects can experience the applied pressure effects before starting the actual MRE acquisition. Subjects should also be trained to keep breathing through the nose in order to maintain the uvula closed. Otherwise, the pressure wave is guided along the upper airways down into the lung, allowing lung MRE but inhibiting brain MRE as waves do not propagate into the brain anymore.

There is not any nominal expected values for *in vivo* shear loss and storage moduli in brain tissues as yet. Nevertheless, the shear viscoelasticity values obtained here by guided pressure wave MRE in the brain are close to those published by some other groups and they increase with the excitation frequency [19, 20, 17, 16, 15, 30]. As shown here and in other groups, data with low displacement field amplitude or noisy data lead to underestimated viscoelastic moduli [47, 28, 35]. Therefore, MRE SNR was introduced and a MRE SNR validity threshold was set over which the viscoelasticity moduli are expected to be correctly extracted [22, 16]. Similarly, the OSS-SNR was introduced [36] and a OSS-SNR validity threshold was set [33]. In this line of thoughts, we have introduced the measurement uncertainty-normalized amplitude of the displacement field ($\mathrm{UNA} = \langle A/\Delta A \rangle$) and we have empirically determined a UNA threshold value over which data in any considered voxel leads to robust mechanical parameters, namely it stands on the plateau that appears while sweeping the amplitude of the applied displacement field. UNA involves both the amplitude and the SNR dependences in the reconstruction process, which then accounts for the sequence sensitivity to motion. On the one hand, the evolution of the mechanical

parameters with either UNA or OSS-SNR follows an exponential growth which asymptotically converges to a plateau. On the other hand, the mechanical parameters are clearly underestimated when UNA or OSS-SNR are lower than the respective thresholds established at the plateaus. These support the findings by McGarry et al. [36] and Murphy et al. [16]. However, neither UNA nor OSS-SNR thresholds are universal and different thresholds are found for the phantom and brain studies. Other parameters, which are not considered by UNA and OSS-SNR, affect the reconstruction of the mechanical parameters. First the ratio between the shear wavelength and the voxel size is critical and should be optimized. Second, the quality of the curl field of the displacement field (UNQ = $\langle q/\Delta q \rangle$) better assesses the requirements for the inversion algorithm used here for reconstruction [35]. Especially when the motion encoding gradient is aligned with the propagating direction of the wave, UNQ might be low while UNA turned to be high. However, for a given experimental protocol (phantom or brain for example), once set, the UNA or OSS-SNR thresholds are steady and can be used further along the implemented protocol.

Two MRE sequences have been applied, one based on a spin-echo (SE) sequence, and a second one based on a gradient-echo using fractional encoding (GRE) with various acquisition parameters to check the mechanical excitation with different available acquisition protocols. We did not intend to establish the best sequence for phantom or brain MRE. The GRE MRE sequence allows shorter acquisition times at the expense of lower motion sensitivity than the SE MRE sequence [38]. To cope with the latter, the amplitude of the generated mechanical waves may be increased, as done in the phantom robustness experiments, where UNA threshold was reached for a higher mean total amplitude with the GRE MRE sequence. Similarly, in brain repeatability experiments, much lower values are obtained for the shear moduli with GRE MRE than with SE MRE. Despite greater wave amplitude for GRE ($\langle A \rangle_{b,\mathrm{GRE}} = (16.0 \pm 9.2)\,\mu\mathrm{m}$ vs $\langle A \rangle_{b,\mathrm{SE}} = (8.3 \pm 4.4)\,\mu\mathrm{m}$), the discrepancy in the shear moduli results from UNA values below threshold for GRE ($\langle \mathrm{UNA} \rangle_{b,\mathrm{GRE}} = 1.7 \pm 0.7$) and above threshold for SE ($\langle \mathrm{UNA} \rangle_{b,\mathrm{SE}} = 5.7 \pm 2.8$). Therefore, it is critical to consider only data for which UNA is above the threshold, which effectively sets the quality and the validity of the MRE outcomes. Otherwise, increasing either the amplitude of the generated displacement field or the sensitivity to motion by cumulative bipolar gradients should be considered. In the frequency study, we did preserve the motion sensitivity by increasing the number of MEG with increasing mechanical frequencies.

5 Conclusion

In this work, we introduced direct pressure waves as a mechanical excitation to circumvent the natural protective barriers and to reach deep organs by following, through the buccal cavity, natural pathways such as the airways for the lungs or the brainstem for the brain. This original approach avoids the main limitation standard techniques face by vibrating the barriers themselves – like the skull or the rib cage – to get the waves through, which implies impairing attenuation before the waves can reach the targeted organ. This robust generator produce shear waves in the entire brain at commonly-used shear wave frequencies in brain MRE ($< 100\,\mathrm{Hz}$). It also extends the possible frequency range to higher frequencies, up to 235 Hz here, as the mechanical parameters could be correctly extracted everywhere but in a few regions only. The frequency range, which can be achieved with such a generator, was limited here to 400 Hz in regard to wave propagation throughout the human brain. It was used in the rat brain up to 521 Hz at 1.5 T [48]. It was expanded to a few kilohertz by a 3.5" dual diaphragm driver in order to perform submillimeter MRE on phantoms and small animals at higher magnetic field and higher mechanical excitation frequency so smaller wavelengths conform to smaller voxel sizes [49]. Endogeneous shear waves generated by the blood pulsation or by any other source could alternatively be used to perform passive MRE [50]. Nevertheless, passive methods are limited to fixed frequencies and they refrain from rheological exploration of human tissue, which can help in mechanically discriminating healthy and diseased tissues [51].

The use of this pressure wave generator can be advantageously extended to lung MRE, simply by breathing through the mouth to steer the pressure waves through the airways. This approach has proven promising and would need further investigation to assess its value in lung applications. Finally, this pressure wave generator can be applied to any other organ or phantom MRE studies by placing the end of the waveguide onto the surface of the subject's skin or of the phantom, such as performed in the breast phantom study here. An output adapter can be implemented to more closely match the surface to be mechanically-excited or to set a definite excitation source, which can be geometrically-limited and easily modelled by a point source [35]. Therein wave geometrical spreading yields attenuation and very small reflected waves – if any – which hinders interference patterns and allow textbook experiments to elicit ongoing phenomena [49, 52].

References

[1] Muthupillai R, Lomas DJ, Rossman PJ, Greenleaf JF, Manduca A, Ehman RL. Magnetic resonance elastography by direct visualization of propagating acoustic strain waves *Science.* 1995;269:1854-1857.

[2] Manduca A., Oliphant T.E., Dresner M.A., et al. Magnetic resonance elastography: Non-invasive mapping of tissue elasticity *Medical Image Analysis.* 2001;5:237 - 254.

[3] Sinkus R., Tanter M., Catheline S., et al. Imaging anisotropic and viscous properties of breast tissue by magnetic resonance-elastography *Magnetic Resonance in Medicine.* 2005;53:372–387.

[4] Van Houten Elijah E.W., Miga Michael I., Weaver John B., Kennedy Francis E., Paulsen Keith D.. Three-dimensional subzone-based reconstruction algorithm for MR elastography *Magnetic Resonance in Medicine.* 2001;45:827–837.

[5] Huwart Laurent, Peeters Frank, Sinkus Ralph, et al. Liver fibrosis: non-invasive assessment with MR elastography *NMR in Biomedicine.* 2006;19:173–179.

[6] Yin Meng, Talwalkar Jayant A., Glaser Kevin J., et al. Assessment of Hepatic Fibrosis With Magnetic Resonance Elastography *Clinical Gastroenterology and Hepatology.* 2007;5:1207 - 1213.e2.

[7] Arani Arvin, Plewes Donald, Krieger Axel, Chopra Rajiv. The feasibility of endorectal MR elastography for prostate cancer localization *Magnetic Resonance in Medicine.* 2011;66:1649–1657.

[8] Yuan Le, Glaser Kevin J, Rouviere Olivier, et al. Preliminary assessment of one-dimensional MR elastography for use in monitoring focused ultrasound therapy *Physics in Medicine and Biology.* 2007;52:5909.

[9] Chen Jun, Woodrum David A., Glaser Kevin J., Murphy Matthew C., Gorny Krzysztof, Ehman Richard. Assessment of in vivo laser ablation using MR elastography with an inertial driver *Magnetic Resonance in Medicine.* 2014;72:59–67.

[10] Salameh N., Diguet E., Souris L., et al. In vivo Monitoring of laser-thermotherapy using MR Elastography in the rat brain in *Proceedings of the 29th Annual Scientific Meeting of the European Society of Magnetic Resonance in Medicine and Biology (Lisboa, Portugal); p. 135*Magn Reson Mat Phys Biol Med 2012.

[11] Sack Ingolf, Beierbach Bernd, Hamhaber Uwe, Klatt Dieter, Braun Jürgen. Non-invasive measurement of brain viscoelasticity using magnetic resonance elastography *NMR Biomed..* 2008;21:265–271.

[12] Green Michael A., Bilston Lynne E., Sinkus Ralph. In vivo brain viscoelastic properties measured by magnetic resonance elastography *NMR Biomed..* 2008;21:755–764.

[13] Hamhaber Uwe, Klatt Dieter, Papazoglou Sebastian, et al. In vivo magnetic resonance elastography of human brain at 7 T and 1.5 T *J. Magn. Reson. Imaging.* 2010;32:577–583.

[14] Latta Peter, Gruwel Marco L.H., Debergue Patricia, Matwiy Brendon, Sboto-Frankenstein Uta N., Tomanek Boguslaw. Convertible pneumatic actuator for magnetic resonance elastography of the brain *Magnetic Resonance Imaging.* 2011;29:147 - 152.

[15] Clayton Erik H., Genin Guy M., Bayly Philip V.. Transmission, attenuation and reflection of shear waves in the human brain *Journal of The Royal Society Interface.* 2012;9:2899–2910.

[16] Murphy Matthew C., Huston John, Jack Clifford R., et al. Measuring the Characteristic Topography of Brain Stiffness with Magnetic Resonance Elastography *PLoS ONE.* 2013;8:e81668.

[17] Johnson Curtis L., Holtrop Joseph L., McGarry Matthew D.J., et al. 3D multislab, multishot acquisition for fast, whole-brain MR elastography with high signal-to-noise efficiency *Magnetic Resonance in Medicine.* 2014;71:477–485.

[18] Braun Jürgen, Guo Jing, Lützkendorf Ralf, et al. High-resolution mechanical imaging of the human brain by three-dimensional multifrequency magnetic resonance elastography at 7T *NeuroImage.* 2014;90:308-314.

[19] Petrov Andrii Y., Sellier Mathieu, Docherty Paul D., Chase J. Geoffrey. Parametric-based brain Magnetic Resonance Elastography using a Rayleigh damping material model *Computer Methods and Programs in Biomedicine.* 2014;116:328 - 339.

[20] Klatt Dieter, Johnson Curtis L., Magin Richard L.. Simultaneous, multidirectional acquisition of displacement fields in magnetic resonance elastography of the in vivo human brain *Journal of Magnetic Resonance Imaging.* 2015;42:297–304.

[21] Murphy Matthew C., Huston John, Jack Clifford R., et al. Decreased brain stiffness in Alzheimer's disease determined by magnetic resonance elastography *J. Magn. Reson. Imaging.* 2011;34:494–498.

[22] Kruse Scott A., Rose Gregory H., Glaser Kevin J., et al. Magnetic resonance elastography of the brain *NeuroImage.* 2008;39:231 - 237.

[23] Anderson Aaron T., Houten Elijah E.W. Van, McGarry Matthew D.J., et al. Observation of direction-dependent mechanical properties in the human brain with multi-excitation {MR} elastography *Journal of the Mechanical Behavior of Biomedical Materials.* 2016;59:538 - 546.

[24] Sakai N., Takehara Y., Yamashita S., et al. Shear Stiffness of 4 Common Intracranial Tumors Measured Using MR Elastography: Comparison with Intraoperative Consistency Grading *American Journal of Neuroradiology.* 2016;37:1851-1859.

[25] Wuerfel Jens, Paul Friedemann, Beierbach Bernd, et al. MR-elastography reveals degradation of tissue integrity in multiple sclerosis *NeuroImage.* 2010;49:2520 - 2525.

[26] Streitberger Kaspar-Josche, Wiener Edzard, Hoffmann Jan, et al. In vivo viscoelastic properties of the brain in normal pressure hydrocephalus *NMR Biomed..* 2011;24:385–392.

[27] Romano Anthony, Scheel Michael, Hirsch Sebastian, Braun Jürgen, Sack Ingolf. In vivo waveguide elastography of white matter tracts in the human brain *Magnetic Resonance in Medicine.* 2012;68:1410–1422.

[28] Guo Jing, Hirsch Sebastian, Fehlner Andreas, et al. Towards an Elastographic Atlas of Brain Anatomy *PLoS ONE.* 2013;8:e71807.

[29] Uffmann K., Maderwald S., Greiff A., Ladd M. E.. Determination of Gray and White Matter Elasticity with MR Elastography in *Proceedings of the 12th Meeting of the International Society for Magnetic Resonance in Medicine (Kyoto); 1768* 2004.

[30] Zhang John, Green Michael A., Sinkus Ralph, Bilston Lynne E.. Viscoelastic properties of human cerebellum using magnetic resonance elastography *Journal of Biomechanics.* 2011;44:1909 - 1913.

[31] Goss B.C., McGee K.P., Ehman E.C., Manduca A., Ehman R.L.. Magnetic resonance elastography of the lung: Technical feasibility *Magn. Reson. Med..* 2006;56:1060–1066.

[32] Mariappan Yogesh K., Glaser Kevin J., Hubmayr Rolf D., Manduca Armando, Ehman Richard L., McGee Kiaran P.. MR elastography of human lung parenchyma: Technical development, theoretical modeling and in vivo validation *Journal of Magnetic Resonance Imaging.* 2011;33:1351–1361.

[33] McGarry M. D. J., Van Houten E. E. W., Johnson C. L., et al. Multiresolution MR elastography using nonlinear inversion *Medical Physics.* 2012;39:6388–6396.

[34] Fehlner Andreas, Papazoglou Sebastian, McGarry Matthew D., et al. Cerebral multifrequency MR elastography by remote excitation of intracranial shear waves *NMR in Biomedicine.* 2015;28:1426–1432. NBM-15-0070.R2.

[35] Yue Jin Long, Tardieu Marion, Julea Felicia, et al. Acquisition and reconstruction conditions in silico for accurate and precise magnetic resonance elastography *Physics in Medicine & Biology.* 2017;62:8655.

[36] McGarry M D J, Houten E E W Van, Perriñez P R, Pattison A J, Weaver J B, Paulsen K D. An octahedral shear strain-based measure of SNR for 3D MR elastography *Physics in Medicine and Biology.* 2011;56:N153.

[37] Sinkus R, Lorenzen J, Schrader D, Lorenzen M, Dargatz M, Holz D. High-resolution tensor MR elastography for breast tumour detection *Physics in Medicine and Biology.* 2000;45:1649.

[38] Rump Jens, Klatt Dieter, Braun Jürgen, Warmuth Carsten, Sack Ingolf. Fractional encoding of harmonic motions in MR elastography *Magn. Reson. Med..* 2007;57:388–395.

[39] Garteiser Philippe, Sahebjavaher Ramin S., Ter Beek Leon C., et al. Rapid acquisition of multifrequency, multislice and multidirectional MR elastography data with a fractionally encoded gradient echo sequence *NMR Biomed..* 2013;26:1326-1335.

[40] Conturo Thomas E., Smith Gregory D.. Signal-to-noise in phase angle reconstruction: Dynamic range extension using phase reference offsets *Magnetic Resonance in Medicine.* 1990;15:420–437.

[41] Gudbjartsson H, Patz S. The Rician distribution of noisy MRI data *Magn. Reson. Med..* 1996;34:910-914.

[42] Oudry Jennifer, Vappou Jonathan, Choquet Philippe, Willinger Rémy, Sandrin Laurent, Constantinesco André. Ultrasound-based transient elastography compared to magnetic resonance elastography in soft tissue-mimicking gels ;54:6979–6990. Publisher: IOP Publishing.

[43] Tardieu M., Poirier-Quinot M., Lamain E., Sinkus R, Darrasse L., Maître X.. Motion correction in MR-Elastography in *Proceedings of the 21st Meeting of the International Society of Magnetic Resonance in Medicine (Salt Lake City); 3099* 2013.

[44] Tardieu M., Poirier-Quinot M., Sinkus R, Darrasse L., Maître X.. Displacement field normalization in MR-elastography: phantom validation and in vivo application in *Proceedings of the 22nd Meeting of the International Society of Magnetic Resonance in Medicine (Milan); 6797* 2014.

[45] McGrath Deirdre M., Ravikumar Nishant, Wilkinson Iain D., Frangi Alejandro F., Taylor Zeike A.. Magnetic resonance elastography of the brain: An in silico study to determine the influence of cranial anatomy *Magnetic Resonance in Medicine.* 2016;76:645–662.

[46] Yang Bin, Shi Zheng, Wang Qun, et al. Frequency spectrum of the human head–neck to mechanical vibrations *Journal of Low Frequency Noise, Vibration and Active Control.* 2018;37:611-618.

[47] Papazoglou S, Hamhaber U, Braun J, Sack I. Algebraic Helmholtz inversion in planar magnetic resonance elastography *Physics in Medicine and Biology.* 2008;53:3147.

[48] Salameh N., Souris L., Sarracanie M., et al. Feasibility of brain MR-Elastography at 1.5 T with a novel wave generator: An animal study in *Proceedings of the 19^{th} Scientific Meeting of the International Society for Magnetic Resonance in Medicine, ISMRM 2011, Montréal, Canada; p. 3492*Magn Reson Med 2011.

[49] Julea Felicia, Yue Jin Long, Boucneau Tanguy, et al. Optimal spatial resolution for accuracy and precision in simulated and experimental micro-MRE at 11.7 T in *Proceedings of the 25^{th} Scientific Meeting of the International Society for Magnetic Resonance in Medicine, ISMRM 2017, Hawai, USA*Magn Reson Med 2017.

[50] Zorgani Ali, Souchon Rémi, Dinh Au-Hoang, et al. Brain palpation from physiological vibrations using MRI *Proceedings of the National Academy of Sciences.* 2015;112:12917-12921.

[51] Van Beers Bernard E., Daire Jean-Luc, Garteiser Philippe. New imaging techniques for liver diseases *Journal of Hepatology.* 2015;62:690 - 700.

[52] Yue Jin Long, Tardieu Marion, Julea Felicia, Leenhardt Lionel, Maître Xavier, Pellot-Barakat Claire. Comparing MR and Ultrasound Shear Wave elasticity measurements in heterogeneous media in *International Tissue Elasticity Conference, ITEC 2015, Verona, Italy* 2015.

List of Figures

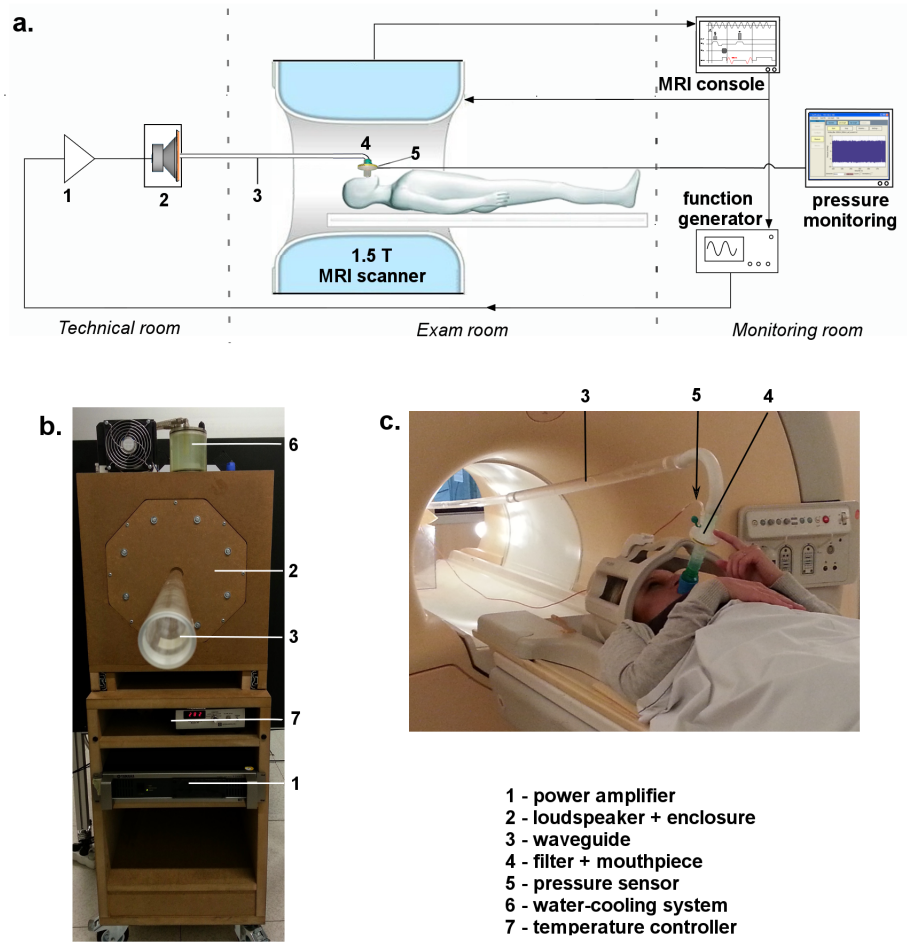

Figure 1: Guided pressure wave MRE setup. (a) Mechanical vibrations are induced in the cerebral by guided pressure waves, remotely generated by a subwoofer (2) connected to a power amplifier (1), placed in a rolling cabinet in the technical room, behind the examination room (b). Pressure waves are transmitted to the subject's buccal cavity by a waveguide (3) through an antibacterial filter and a mouthpiece (4). (c) An optical pressure sensor (5), connected to the antibacterial filter, allows to monitor the pressure at the mouth.

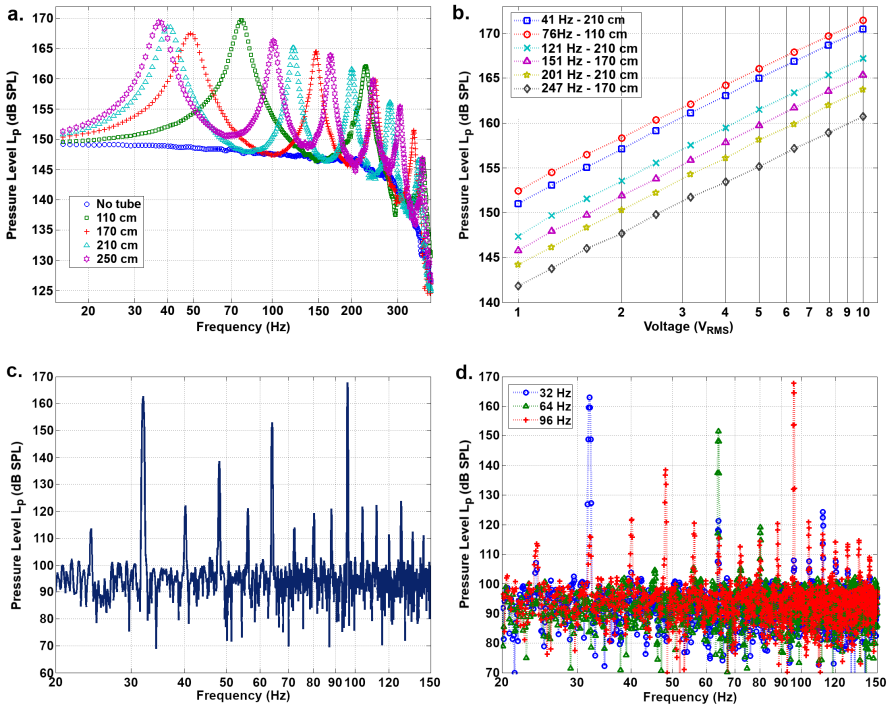

Figure 2: Top row: Transducer characterization. The pressure level was recorded for vibration frequencies from 0 to 400 Hz at the end of the waveguide in a closed configuration when using different waveguide lengths ($\{0, 1.10, 1.70, 2.10, 2.50\}$ m) and different input voltages (1-10 V). (a) Frequency response curves for 5 waveguide lengths, with an input voltage of 8 V_{RMS}. (b) Pressure levels as functions of the input voltage for six resonance frequencies and their corresponding waveguide lengths.
Bottom row: transducer characterization for multifrequency MRE. Transducer frequency response was recorded at the end of a 250 cm waveguide in a closed configuration when three harmonic frequencies, 32 Hz, 64 Hz and 96 Hz, were applied simultaneously (c) or separately (d).

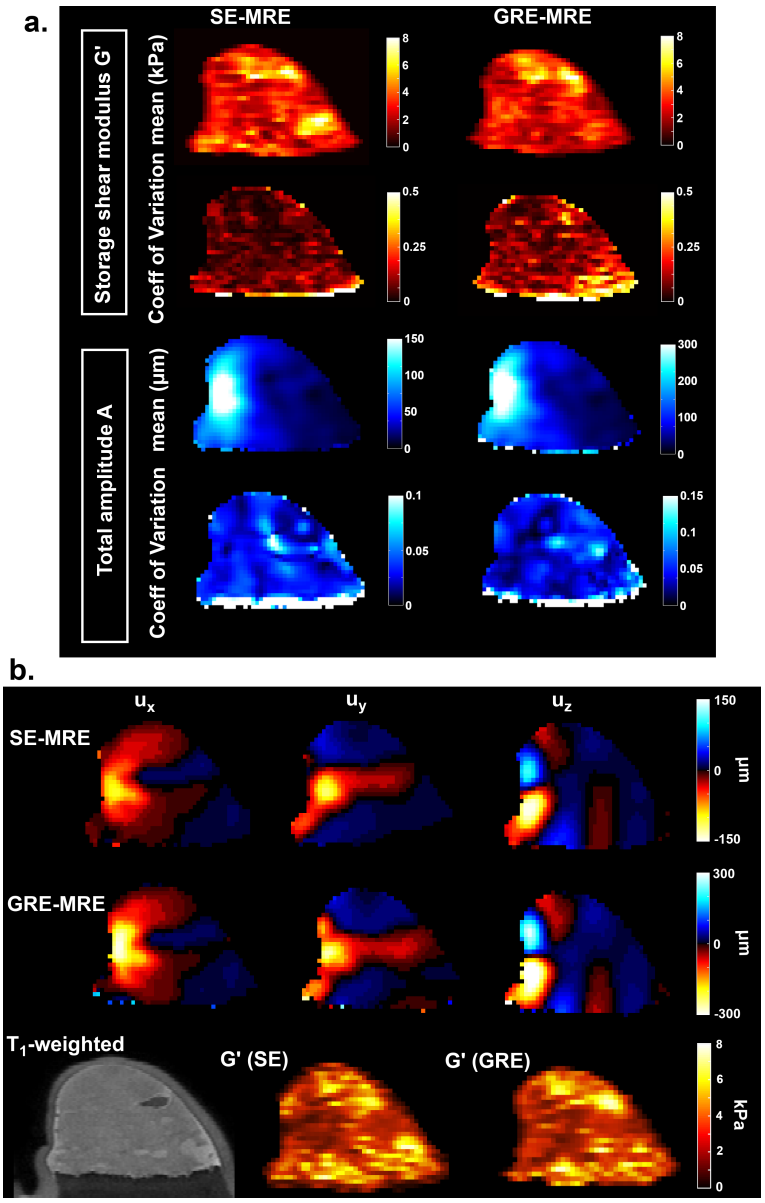

Figure 3: Phantom Results. (a) Storage modulus, G', and total amplitude, A, mean and coefficient of variation maps measured over five repeated acquisitions. (b) Displacement field maps at a central axial slice of the phantom for SE (upper row) and GRE (middle row) MRE sequences along x (Ux), y (Uy) and z (Uz) directions for a given time offset and for one of the five repeated acquisitions. Corresponding T_1-weighted image and G' maps for SE and GRE MRE sequences (lower row)

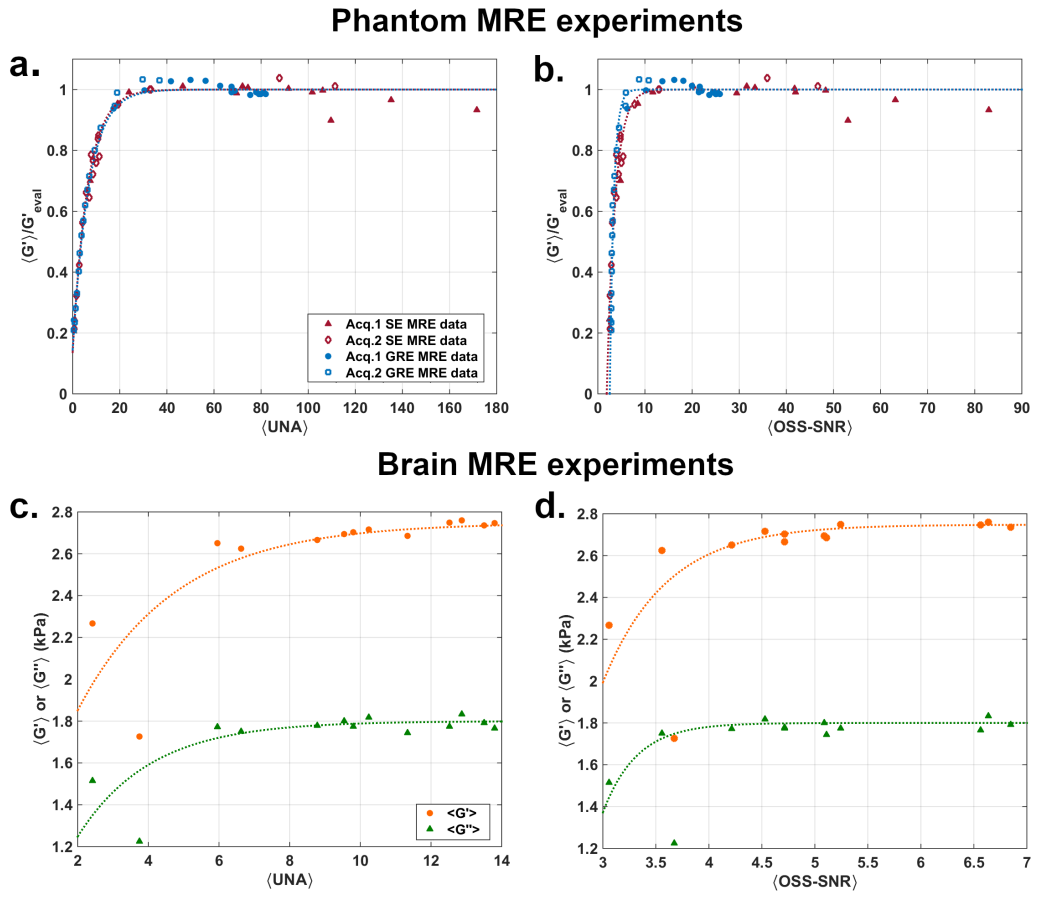

Figure 4: Robustness results. Top row: Normalized mean G' values of the whole phantom as a function of UNA (a) and OSS-SNR (b), for the acquired SE (red plots) and GRE (blue plots) MRE data with the associated fitted model (dotted curves). Both SE and GRE MRE data were acquired twice at different times (triangle and circle plots for the first acquisition, and diamond and square plots for the second acquisition).
Bottom row: Mean G' (orange circle) and G'' (green triangle) values of brain SE MRE acquisitions, plotted as functions of UNA (c) and OSS-SNR (d) with the associated fitted model (dotted curves).

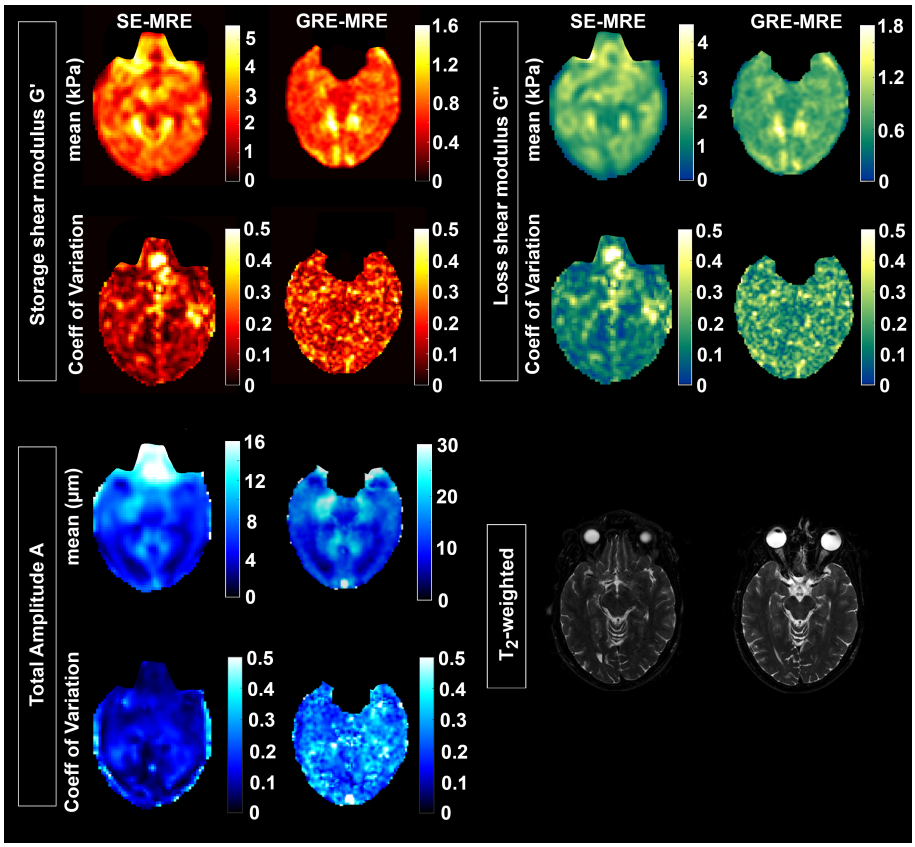

Figure 5: Repeatability study. Storage modulus, G', loss modulus, G'', and total amplitude, A, maps averaged over five repeated brain acquisitions in the same subject with their coefficient of variation maps and corresponding T_2-weighted images. For SE and GRE MRE sequences and a mechanical excitation of 83 Hz.

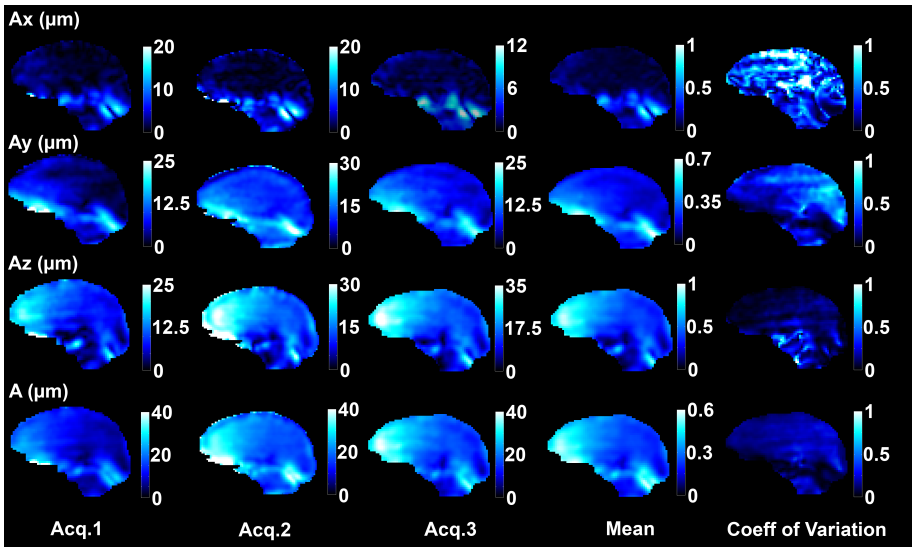

Figure 6: Reproducibility study. Amplitude maps for the x (right-left, Ax), y (anteroposterior, Ay) and z (feet-head, Az) directions and total amplitude map (A), for three whole brain acquired data: acq.1, acq.2 and acq.3, realized on the same subject and acquisition parameters, at different times. For a sagittal slice. Mean maps measured over the three normalized acquired data with corresponding coefficient of variation maps are presented, for each amplitude maps.

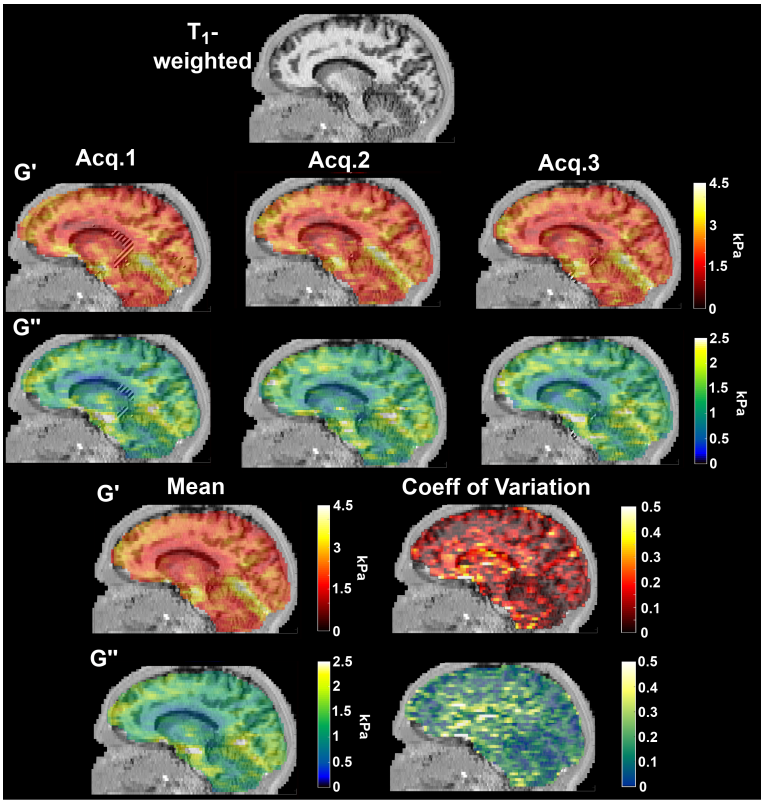

Figure 7: Frequency study. G' and G'' maps for the three whole brain acquisitions, acq.1 (left), acq.2 (middle) and acq.3 (right), with corresponding anatomic sagittal slice (T_1-weighted). Bottom: Mean and coefficient of variation maps of G' and G'' extracted from three MRE acquisitions realized on the same subject and with the same acquisition parameters, at different times. Pixel below the threshold of UNA are shown striped on the G' and G'' maps.

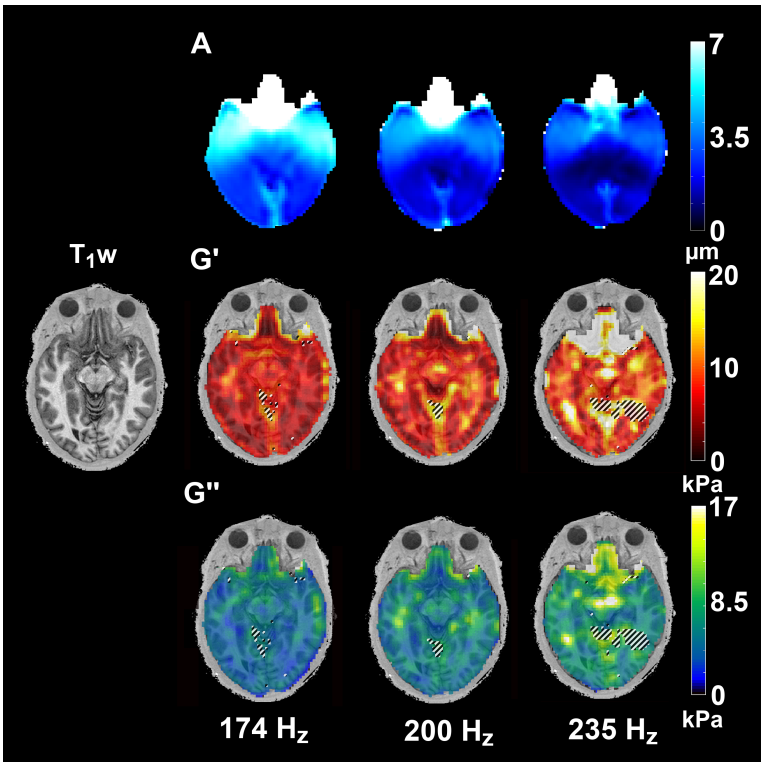

Figure 8: Total amplitude (A), G' and G'' of three MRE acquisitions of the same subject with excitation frequencies of 174 Hz, 200 Hz and 235 Hz. Pixel values below the threshold of UNA are shown striped on the G' and G'' maps.